Distributed strain measurement and possible breakage detection of optical-fiber-embedded composite structure using slope-assisted Brillouin optical correlation-domain reflectometry

Heeyoung Lee[1*], Yutaka Ochi[2], Takahiro Matsui[3], Yukihiro Matsumoto[4], Yosuke Tanaka[5], Hitoshi Nakamura[6], Yosuke Mizuno[1], and Kentaro Nakamura[1]

[1]Institute of Innovative Research, Tokyo Institute of Technology, Yokohama 226-8503, Japan
[2]Advanced Composites Center, Toray Industries, Inc., Nagoya 455-0024, Japan
[3]First Advanced Composites Technical Department, Toray Industries, Inc., Nagoya 455-0024, Japan
[4]Department of Architecture and Civil Engineering, Toyohashi University of Technology, Toyohashi, Aichi 441-8580, Japan
[5]Institute of Engineering, Tokyo University of Agriculture and Technology, Koganei, Tokyo 184-8588, Japan
[6]Department of Civil and Environmental Engineering, Tokyo Metropolitan University, Hachioji, Tokyo 192-0397, Japan

*E-mail: hylee@sonic.pi.titech.ac.jp

Slope-assisted Brillouin optical correlation-domain reflectometry (SA-BOCDR) is a recently developed structural health monitoring technique for measurements of strain, temperature, and loss distributions along optical fibers. Although the basic operational principle of this method has been clarified, no measurements using optical fibers embedded in actual structures have been reported. As a first step towards such practical applications, in this study, we present an example of an SA-BOCDR-based diagnosis using a composite structure with carbon fiber-reinforced plastics. The system's output agrees well with the actual strain distributions. We were also able to detect the breakage of the embedded fiber, thus demonstrating the promise of SA-BOCDR for practical applications. © 2018 The Japan Society of Applied Physics

Recently, the demand for structural health monitoring of deteriorated or damaged civil infrastructures has been rapidly growing. Many types of sensing techniques have been suggested to improve human safety and maintainability of infrastructures. As one of the methods to achieve this goal, Brillouin-scattering-based optical fiber sensing techniques[1–15] have attracted a significant attention owing to their ability to measure strain and temperature distributions. Among various Brillouin sensors,[1–6] Brillouin optical correlation-domain reflectometry (BOCDR)[5] is the only technique that can simultaneously achieve single-end access, random access, high spatial resolution, and cost efficiency. However, one of the major drawbacks of BOCDR has been its relatively large measurement time, owing to the frequency sweeping function required for the acquisition of the Brillouin gain spectrum (BGS). In order to overcome this drawback, we have recently developed two types of frequency-sweeping-free BOCDR configurations: phase-detected (PD) BOCDR[16] and slope-assisted (SA) BOCDR.[17] PD-BOCDR can offer sampling rates over 100 kHz; however, the measurable maximum strain is limited to ∼0.2%. In this study, we focus on SA-BOCDR, which can be used to measure larger strains [although its strain dynamic range is also restricted by the BGS shape and Brillouin-frequency-shift (BFS) dependence on the strain].

In order to measure the strain, temperature, and local loss, SA-BOCDR utilizes not the BFS but the power on the slope of the BGS. In addition to its high-speed operation, this configuration offers the so-called beyond-nominal-resolution effect.[18] By employing this effect, a strained or heated section even several tens of times shorter than the nominal spatial resolution can be detected. We have already demonstrated the detection of a 2-mm-long strained section;[19] this is the smallest length that has ever been experimentally detected using distributed Brillouin sensors. The use of a polymer optical fiber (POF) with an extremely high flexibility and high temperature sensitivity as a sensing fiber of SA-BOCDR has also been shown to be effective.[20] Therefore,

the performance of SA-BOCDR has significantly improved; however, its relevance to optical fibers embedded in actual structures has not yet been experimentally demonstrated, which is of crucial importance to its applicability.

In this study, as a first step towards such practical applications, we present an example of an SA-BOCDR-based diagnosis using an optical fiber embedded in a composite structure. As a specimen to be measured, we prepared a carbon-fiber-reinforced-plastic (CFRP)[21–23]-strengthened steel plate, in which a standard silica single-mode fiber (SMF; not a POF) was embedded. Upon application of load to the structure on its top or bottom, we detect the induced compressive or tensile strain distributions, respectively. We show that the breakage of the embedded fiber can also be detected as an abrupt local power change in the SA-BOCDR output.

Owing to their high strength, high elastic modulus, small weight, and high corrosion resistance, CFRPs have been widely used as materials to repair or strengthen steel structures.[24] In this experiment, as a specimen, a CFRP-strengthened steel plate was prepared using the vacuum-assisted resin transfer molding (VaRTM) technique,[25–27] which is known as an advanced, highly reliable, and reproducible method for the fabrication of composite materials. The VaRTM process is schematically shown in Fig. 1.[26] The process was performed by infusing liquid resin into laminated fibers or woven fabrics using a pressure differential between the atmosphere and vacuum; thereafter, the resin was hardened by heat (see Ref. 25 for more details). This technique does not require a prepreg or autoclave, yielding a highly efficient fabrication of composite materials.

Figure 2 shows the structure of the specimen. A 1.4-m-long silica SMF with a BFS of 10.85 GHz at room temperature (23 °C) was, as a sensing fiber, embedded between a steel plate and CFRP strips [containing carbon fiber cloth (Torayca UM46-40G)]. This structure was fabricated by placing the SMF before the infusion of liquid resin during the VaRTM process. The depth of the structure (both steel plate
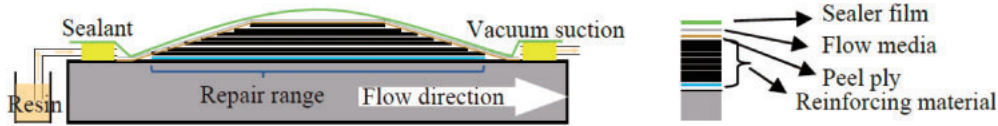
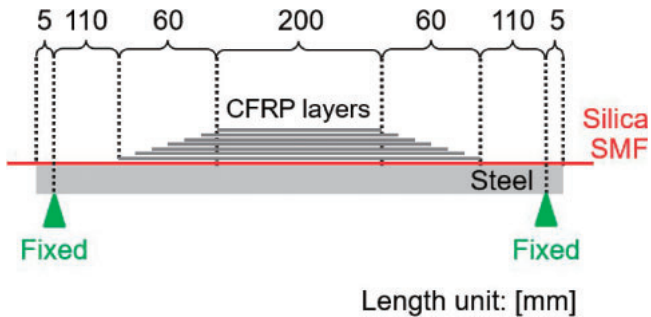**Fig. 1.** Schematic of the VaRTM process (adapted from Ref. 26).
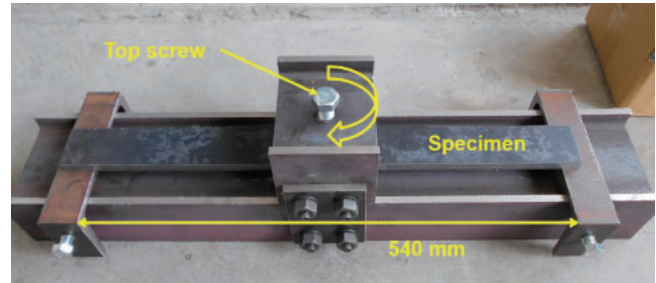

Fig. 2. Structure of the specimen.

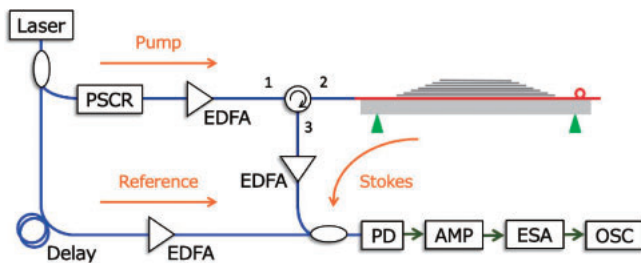
Fig. 4. Three-point bending device.

Fig. 3. Experimental setup for SA-BOCDR. EDFA: erbium-doped fiber amplifier, ESA: electrical spectrum analyzer, OSC: oscilloscope, PD: photo detector, PSCR: polarization scrambler.

and CFRP strips) was 39 mm, while the thickness of the steel plate was 12 mm. The total thickness of the CFRP strips composed of seven tapered layers (the length of each strip differed by 10 mm) was ~3 mm.

Figure 3 shows the experimental setup of SA-BOCDR for the measurement of the strain distributions along the sensing fiber, which was basically equal to that used in our previous study.[17] The 1,550-nm light from a semiconductor laser was divided into two light beams: incident and reference. After passing through a polarization scrambler (PSCR), the incident light was amplified to ~28 dBm using an erbium-doped fiber amplifier (EDFA) and injected into the sensing fiber embedded in the specimen. In the meantime, the reference light was guided to a 1-km-long delay fiber, amplified to ~3 dBm, and then heterodyned with the Stokes light (Brillouin-scattered from the sensing fiber; amplified to ~1 dBm). The heterodyned optical signal was converted into an electrical signal using a photo detector (PD), and amplified by 23 dB using an electrical amplifier to improve the signal–to–noise ratio (SNR). Thereafter, the spectral power change at a fixed frequency ν_{B0} (= 10.83 GHz)[17] of the BGS was acquired using the narrow band-pass filtering function of an electrical spectrum analyzer (ESA) and observed using an oscilloscope (OSC). The video and resolution bandwidths of the ESA were 3 kHz and 10 MHz, respectively. Averaging was performed 1,024 times to enhance the SNR.

In order to resolve the sensing locations, the laser output frequency was sinusoidally modulated, and a so-called

correlation peak was generated in the sensing fiber.[3,5] By sweeping the modulation frequency f_m (= 9.132–9.156 MHz), the correlation peak was scanned along the fiber, enabling a distributed measurement. The measurement range d_m was 11.3 m, which was determined by f_m according to Eq. (16) in Ref. 28. By setting the modulation amplitude Δf to 1.52 GHz, the spatial resolution of the system was 7.1 cm [calculated from Eq. (15) in Ref. 28].

We performed two different types of experiments: one to evaluate the magnitudes of the tensile and compressive strains applied to the sensing fiber, and the other one to detect the breakage of the fiber. First, using a three-point bending device (Fig. 4), tensile and compressive strains were applied to the middle of the specimen by tightening the top screw with a pitch of 2 mm (the specimen was upturned when tensile strains were applied). We measured the distributed tensile and compressive strains from 0 to 1.5 and from 0 to 2.5 turns (of the top screw), respectively. Measurements were performed every 0.5 turns. According to our calculation based on a finite-element analysis, the strain increases by ~400 $\mu\varepsilon$ with each additional turn, leading to the applied strains of approximately 0, 200, 400, and 600 $\mu\varepsilon$ (for tensile strains) and 0, 200, 400, 600, 800, and 1,000 $\mu\varepsilon$ (for compressive strains).

Similar experiments were performed by applying larger compressive strains to the specimen until the sensing fiber broke. Using SA-BOCDR, the power-change distributions were measured while the top screw was tightened from 0 to 6.0 turns, corresponding to strains of 0 to ~2,400 $\mu\varepsilon$. Throughout the measurements, the room temperature was 23 °C.

First, we present the experimental results of the evaluation of the magnitudes of the applied tensile and compressive strains. Figure 5(a) shows the measured power-change distributions along the whole sensing fiber when the tensile strains of 0, 200, 400, and 600 $\mu\varepsilon$ and compressive strains of 0, 200, 400, 600, 800, and 1,000 $\mu\varepsilon$ were applied to the specimen. The vertical axis was converted into strain using the known strain-dependence coefficient of a power change of −1.59 dB/%.[17] It is worth noting that the positive and negative signs indicate tensile and compressive strains, respectively. The horizontal axis represents the relative distance from the midpoint of the embedded section of the sensing fiber (positive values correspond to distal locations).
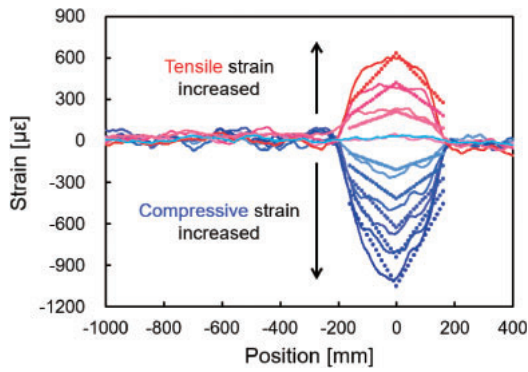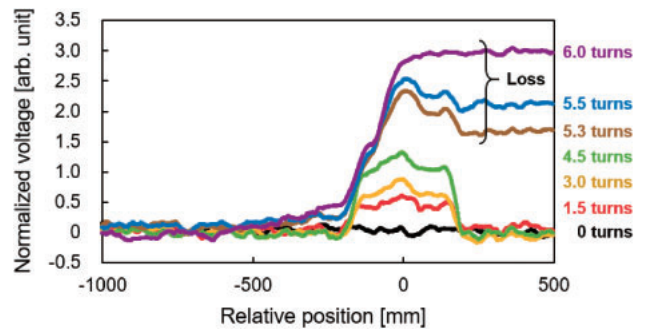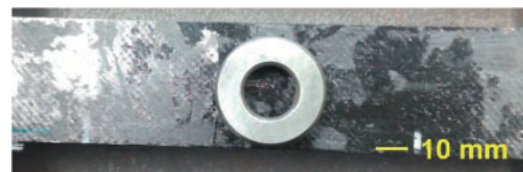
(a)
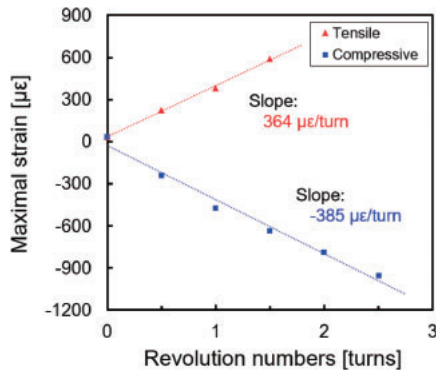
(b)

Fig. 5. (a) Strain distributions measured along the sensing fiber when tensile strains of 0, 200, 400, and 600 $\mu\varepsilon$ and compressive strains of 0, 200, 400, 600, 800, and 1,000 $\mu\varepsilon$ were applied. The dotted lines indicate the theoretical trends. (b) Maximum tensile and compressive strains [derived from (a)] as a function of the revolution number of the top screw.

Fig. 6. Power-change distributions measured along the sensing fiber when the compressive strains were applied until the fiber broke.

(a)

(b)

(c)

Fig. 7. Photographs of the CFRP strips peeled off from the steel; (a) top view, (b, c) side views.

The power changes were observed along an ~390-mm-long section around the embedded section. It is worth noting that the actually embedded length of the sensing fiber was ~320 mm; the difference of ~70 mm corresponds to the nominal spatial resolution.[18] With the increase of the applied tensile and compressive strains, the measured strains also increased moderately, in agreement with the theoretical values (shown by dotted lines; which are not theoretical SA-BOCDR outputs but theoretical strain distributions). In Fig. 5(b), the maximum strain obtained from each measured distribution in Fig. 5(a) is plotted as a function of the number of revolutions of the top screw. Irrespective of tensile or compressive strains, the maximum strain increased almost linearly with the number of revolutions of the screw. The calculated slopes for the tensile and compressive strains were ~364 and ~385 $\mu\varepsilon$/turn, respectively, in a moderate agreement with the theoretical values (~400 $\mu\varepsilon$/turn). The discrepancy seems to be caused by the insufficient adhesion strength of the sensing fiber.

Subsequently, we detected the breakage of the sensing fiber by applying larger compressive strains to the specimen. The top screw was tightened to 0, 1.5, 3.0, 4.5, 5.3, 5.5, and 6.0 turns. The measured distributions of the power change (output as voltage) are shown in Fig. 6. The vertical axis was defined to be positive when the strain was compressive. When the number of revolutions was equal to or smaller than 4.5, the power changes were observed along the correct section (i.e., embedded fiber section). In this range of strains, the power

change was almost proportional to the number of revolutions. However, when the number of revolutions was larger than 5.3 (~2,120 $\mu\varepsilon$), the power change exhibited a significant increase along the distal side from the midpoint of the specimen. This behavior implies that a considerable optical loss was induced,[17] possibly by the fiber breakage. Figure 7 shows photographs of the specimen after the revolution of 6.0 turns. A part of the CFRP strips were clearly peeled off from the steel. These results indicate that SA-BOCDR has the capability to indirectly predict the peeling of composite structures through fiber breakage detection.

In conclusion, we experimentally investigated the strain distributions along the sensing fiber embedded in the CFRP-strengthened steel plate. The measured tensile and compressive strains were linearly dependent on the number of revolutions of the top screw. The dependence coefficients were ~364 $\mu\varepsilon$/turn for tensile strain and ~385 $\mu\varepsilon$/turn for compressive strain, which were in a moderate agreement with the theoretical values. We also detected the breakage of the embedded sensing fiber when large compressive strains were applied. The optical loss appeared when the screw was tightened to 5.3 turns (~2,120 $\mu\varepsilon$); the embedded sensing

fiber was completely broken at 6.0 turns ($\sim$2,400 $\mu\varepsilon$). We believe that, by presenting a promising example of composite structural diagnosis, this study provides an important basis for the future development of SA-BOCDR-based health monitoring systems for practical applications.

1) T. Horiguchi and M. Tateda, J. Lightwave Technol. **7**, 1170 (1989).
2) T. Kurashima, T. Horiguchi, H. Izumita, S. Furukawa, and Y. Koyamada, IEICE Trans. Commun. **E76-B**, 382 (1993).
3) D. Garus, T. Gogolla, K. Krebber, and F. Schliep, Opt. Lett. **21**, 1402 (1996).
4) K. Hotate and T. Hasegawa, IEICE Trans. Electron. **E83-C**, 405 (2000).
5) Y. Mizuno, W. Zou, Z. He, and K. Hotate, Opt. Express **16**, 12148 (2008).
6) A. Minardo, R. Bernini, R. Ruiz-Lombera, J. Mirapeix, J. M. Lopez-Higuera, and L. Zeni, Opt. Express **24**, 29994 (2016).
7) Y. Dong, L. Chen, and X. Bao, Opt. Lett. **36**, 277 (2011).
8) H. Ohno, H. Naruse, M. Kihara, and A. Shimada, Opt. Fiber Technol. **7**, 45 (2001).
9) K. Hotate and T. Yamaguchi, Jpn. J. Appl. Phys. **44**, L1030 (2005).
10) D. Garus, T. Gogolla, K. Krebber, and F. Schliep, J. Lightwave Technol. **15**, 654 (1997).
11) W. Zou, Z. He, and K. Hotate, IEEE Sens. J. **14**, 244 (2014).
12) R. Bernini, A. Minardo, and L. Zeni, IEEE Photonics J. **4**, 48 (2012).
13) N. Hayashi, Y. Mizuno, and K. Nakamura, IEEE Photonics J. **6**, 6803108 (2014).
14) J. Urricelqui, A. Zornoza, M. Sagues, and A. Loayssa, Opt. Express **20**, 26942 (2012).
15) D. Zhou, Y. Dong, B. Wang, and H. Li, Opt. Express **25**, 1889 (2017).
16) Y. Mizuno, N. Hayashi, H. Fukuda, K. Y. Song, and K. Nakamura, Light: Sci. Appl. **5**, e16184 (2016).
17) H. Lee, N. Hayashi, Y. Mizuno, and K. Nakamura, IEEE Photonics J. **8**, 6802807 (2016).
18) H. Lee, N. Hayashi, Y. Mizuno, and K. Nakamura, Opt. Express **24**, 29190 (2016).
19) H. Lee, Y. Mizuno, and K. Nakamura, Jpn. J. Appl. Phys. **57**, 020303 (2018).
20) H. Lee, N. Hayashi, Y. Mizuno, and K. Nakamura, J. Lightwave Technol. **35**, 2306 (2017).
21) D. G. Pearce, Fibre Sci. Technol. **3**, 129 (1970).
22) U. Meier, Struct. Eng. Int. **2**, 7 (1992).
23) C. Soutis, Mater. Sci. Eng. A **412**, 171 (2005).
24) S. Rizkalla, M. Dawood, and D. Schnerch, Composites, Part A **39**, 388 (2008).
25) H. Nakamura, R. Kondo, T. Matsui, and Y. Matsumoto, Proc. Int. Conf. FRP Composites in Civil Engineering (CICE), 2016, p. 438.
26) G. Mieda, H. Nakamura, T. Matsui, Y. Ochi, Y. Mizuno, K. Nakamura, and Y. Matsumoto, Proc. Asia–Pacific Conf. FRP in Structures (APFIS), 2017, P78.
27) C. Dong, Composites, Part A **37**, 1316 (2006).
28) Y. Mizuno, W. Zou, Z. He, and K. Hotate, J. Lightwave Technol. **28**, 3300 (2010).